

Ultrafast Resonant Dynamics of Surface Plasmons in Gold Nanorods

Sungnam Park,^{†,§} Matthew Pelton,^{‡,||} Mingzhao Liu,[†] Philippe Guyot-Sionnest,^{†,‡} and Norbert F. Scherer^{*,†}

Departments of Chemistry and Physics, University of Chicago, 5735 South Ellis Avenue, Chicago, Illinois 60637

Received: April 30, 2006; In Final Form: August 25, 2006

Electron dynamics in Au nanorods are studied with femtosecond nonlinear spectroscopic techniques, by directly exciting and probing the longitudinal surface plasmon resonance. The dispersive and absorptive parts of the third-order signal are measured using optical heterodyne detected four-wave-mixing spectroscopy. These signals are used to describe dynamics in Au nanorods in terms of frequency shift and broadening of the plasmon resonance. Pump–probe experiments are performed with a series of pump intensities. The results are treated in two ways: (1) by calculating the temperature changes of electrons and phonons in the nanorods and the effects of these temperatures on the dielectric constant of Au; and (2) by a nonlinear least-squares fitting using a phenomenological response function. The first model agrees with the pump–probe experimental results for pump energies up to 2.0 nJ (2.5 GW/cm²) and for delays in the range of 150 fs to 150 ps, but does not reproduce three additional features present in the data and the phenomenological model: (1) an “instantaneous” response, attributed to coherent plasmon oscillation; (2) a decaying component with an intensity-independent time constant of 170 fs, attributed to a nonthermal electron distribution or to two-photon-excited interband transitions; and (3) oscillations with a period of 71 ps, attributed to coherent vibration of the rods. Higher pump intensities yield substantial deviation at short delays from the lower-intensity response. Additional plasmon damping and higher-order nonlinear mechanisms are suggested to account for these deviations.

1. Introduction

Optical excitation of appropriately shaped metal nanoparticles can result in very large local fields that can, in turn, give rise to substantial nonlinear optical effects.^{1,2} The large local fields are the result of the surface plasmon (SP) resonance, the collective oscillation of conduction-band electrons in the nanoparticles. The frequency and bandwidth of the SP resonance depends on the size and shape of the nanoparticles as well as their dielectric constant and that of the surrounding medium.³ For nanorods, the SP resonance splits into two bands: parallel (longitudinal) and perpendicular (transverse) to the long axis of the nanorod. As the aspect ratio of the rod increases, the energy separation between the two SP resonance frequencies increases, the longitudinal SP resonance being lower in energy than the transverse SP resonance.

Electron dynamics in metal films and metallic nanoparticles have previously been investigated by femtosecond nonlinear spectroscopy.^{4–14} The electron distribution is perturbed by a short pump pulse, and the resulting relaxation to a new equilibrium distribution is monitored by a time-delayed probe pulse. Several processes contribute to the dynamics, including internal electron thermalization, electron–phonon scattering, and phonon–phonon scattering. Electron relaxation dynamics have been studied using near-infrared pump pulses, which perturb the electron distribution in the conduction band, and near-UV

or visible probe pulses near the interband transition threshold.^{4,9–11,15,16} Alternatively, near-UV or visible pump pulses have been used to excite electrons via intraband and interband transitions, and transient-absorption spectra have been measured around the surface-plasmon resonance by probing with a white-light continuum.^{5–7,13,14,17–19}

The present paper is a study of the electron dynamics in Au nanorods by direct and selective excitation and probing of the longitudinal SP mode. The energy of the pump photon is resonant with the longitudinal SP, but is smaller than the energy gap between the d-band and the Fermi level, meaning that direct interband transitions are negligible. The SP resonance absorption can thus be selectively excited and probed.⁷ Pump–probe and optical-heterodyne-detected four-wave-mixing (OHD-FWM) techniques are used, allowing direct measurement of both the dispersive and absorptive parts of the third-order nonlinear optical response. This allows a description of surface-plasmon dynamics in terms of frequency shift and broadening. The pump–probe measurements are performed over a range of pump intensities to determine the dependence of the time constants of electron relaxation in Au nanorods. Significant deviations are observed at high pump intensities.

2. Experimental Section

2.1. Nanorod Sample. For the present measurements, Au nanorods are synthesized by a seed-mediated method.^{20,21} The aspect ratio is affected by the amount and size of seed particles, the pH of the solution, and the concentration of surfactants.

Au seeds are always prepared in the same way and used without any aging. First, 0.25 mL of 10 mM HAuCl₄ is mixed with 10 mL of 0.1 M CTAB (cetyltrimethylammonium bromide) solution at room temperature. A 0.6-mL aliquot of freshly

* To whom correspondence should be addressed. E-mail: nfschere@uchicago.edu.

[†] Department of Chemistry.

[‡] Department of Physics.

[§] Present address: Department of Chemistry, Stanford University, Stanford, CA 94305.

^{||} Present address: Center for Nanoscale Materials, Argonne National Laboratory, 9700 S. Cass Ave., Argonne, IL 60439.

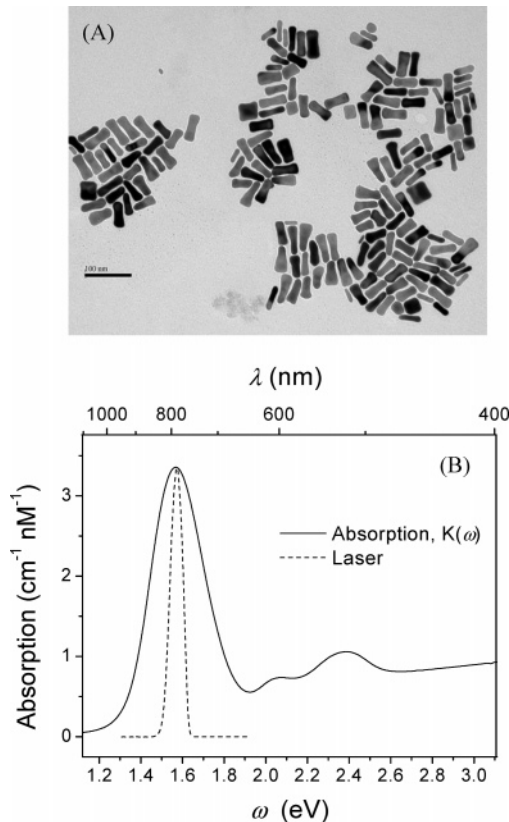


Figure 1. (A) TEM image of Au nanorods used for the ultrafast optical measurements. The scale bar is 100 nm. (B) Absorption spectrum of Au nanorods dispersed in water. The scaled laser spectrum is also shown.

prepared 10 mM NaBH₄ solution is then quickly injected into the Au solution under vigorous stirring. The color of the solution changes from yellow to orange, indicating the formation of Au nanoparticles with diameters smaller than 4 nm. A 50 mL growth solution of 0.1 M CTAB is prepared and kept at about 25 °C. Next, 2.5 mL of 10 mM HAuCl₄ and 0.5 mL of 10 mM AgNO₃ are mixed with the growth solution, and the Au(III) is reduced to Au(I) by injecting 0.4 mL of 0.1 M ascorbic acid. Finally, 0.12 mL of the Au seed solution is injected into the growth solution. The solution is kept overnight under slow stirring. To remove excess surfactant, the prepared Au nanorod solution is first cooled to 5 °C, so that the CTAB can partly crystallize, and is then centrifuged at 3500 rpm for 4 min.

A representative TEM image of the Au nanorods used in the present measurements is shown in Figure 1A. The nanorods have an aspect ratio of 3.76 ± 0.53 (with lengths of 53 ± 7 nm) and are dispersed in water. The measured absorption spectrum of the solution is shown in Figure 1B; the two peaks at 790 and 520 nm correspond to the longitudinal and transverse SP modes, respectively.

2.2. Femtosecond Optical Measurements. A home-built, cavity-dumped Ti:sapphire oscillator is used to generate 20 nJ, ~20 fs pulses centered at a wavelength of 790 nm.²² The pulses are amplified to 1.5 μJ in a home-built cavity-dumped Ti:sapphire amplifier containing chirped mirrors, at repetition rates ranging from 10 to 250 kHz.^{23,24} The pulses are compensated for material dispersion with a pair of BK7 prisms, resulting in 40-fs pulses at the sample position.

Pump-probe transient-transmission and OHD-FWM measurements are employed to investigate the electron dynamics in Au nanorods. The latter method, which was recently implemented with diffractive optics,^{25–29} is used for separate

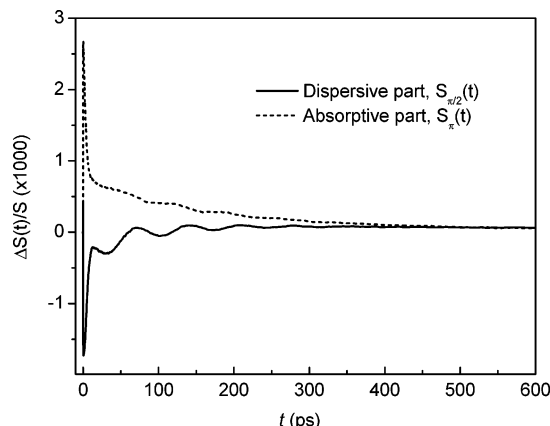


Figure 2. The dispersive, $S_{\pi/2}(t)$, and absorptive, $S_{\pi}(t)$, parts of the optical-heterodyne-detected four-wave-mixing signal. The pulse energies are 0.27 nJ for the probe and 0.54 nJ for the pump.

measurements of the real and imaginary parts of the third-order polarization, $\mathbf{P}^{(3)}(t)$. The details and performance of our OHD-FWM setup will be reported elsewhere.³⁰

For optical measurements, the Au nanorod sample is circulated in a flow cell at a rate of 1 mL/s using a peristaltic pump. The signal is detected with photodiodes (Thorlabs, DET210) and processed with a lock-in amplifier referenced to a chopper in the pump beam, operating at 2.73 kHz. No distortion of the measured signal is observed when increasing the laser-pulse repetition rate from 18 kHz to 124 kHz, although the S/N ratio improves, indicating the absence of an accumulated thermal or photochemical effect. The repetition rate is fixed at 37 kHz for all measurements.

3. Optical-Heterodyne-Detected Four-Wave Mixing Measurements

3.1. Direct Measurements of Dispersive and Absorptive Nonlinearities. Previous time-resolved FWM experiments on Au nanoparticles did not involve a local oscillator field^{31,32} and thus could not separately measure the dispersive and absorptive parts of the signal. The OHD-FWM technique provides a measurement of complex nonlinear signals, allowing a direct determination of the complex refractive index (or complex dielectric function) without resorting to a Kramers-Kronig transformation.^{28,29,33}

The complex refractive index of a system is written as the sum of the dispersive (real) and absorptive (imaginary) parts:

$$N(\omega) = n(\omega) + iK(\omega) \quad (1)$$

The signals measured in the OHD experiments are related to the changes in dispersion, $\Delta n(\omega)$, and absorption, $\Delta K(\omega)$, of the system²⁹

$$\begin{aligned} S(t) &= -[\Delta n(t) + i\Delta K(t)]L \\ &= S_{\pi/2}(t) + iS_{\pi}(t), \end{aligned} \quad (2)$$

where L is the path length and $S_{\pi/2}(t)$ and $S_{\pi}(t)$ are the in-quadrature and in-phase parts of the signal, respectively. Figure 2 shows the time dependence of the dispersive and absorptive parts, measured directly by OHD-FWM method. The dispersive part is negative in magnitude and has a slow oscillatory component, while the absorptive part is positive in magnitude and has the same oscillatory component, but with smaller amplitude.

3.2. Surface Plasmon Resonance Spectral Dynamics. The heating of the electron gas by the injected energy from the laser pulse leads to a frequency shift and spectral broadening of the nanoparticle SP absorption. These, in turn, result in a transient bleach centered at the plasmon band maximum and two induced-absorption wings at lower and higher energies.^{5,9,14} The time-dependent electron distribution leads to time evolution of the transient-absorption spectrum of the Au nanorods, corresponding principally to changes in the center frequency, $\Omega_{\text{SP}}(t)$, and bandwidth, $\gamma_{\text{SP}}(t)$, of the SP absorption.

In the present experiment, the excitation wavelength is away from the interband absorption threshold in Au, which lies at about 2.4 eV (520 nm). Thus, the interband absorption is negligible, and the number of electrons in the conduction band does not change upon excitation. The pump pulse excites electrons within the conduction band, changing the distribution of electrons near the Fermi level. The center frequency and bandwidth of the SP absorption are sensitive to this electron distribution and can thus be used to probe electron dynamics in the nanorods.

The Au nanorod sample has an inhomogeneous distribution of rod aspect ratios resulting in a broad absorption spectrum, as shown in Figure 1. The laser spectrum is narrower than that of the Au nanorod sample, so only a subset of nanorods is selectively excited by the laser pulse. The spectrum of nanorods excited by the laser pulse can be approximated as a Gaussian

$$K_{\text{SP}}(\omega, t < 0) = \frac{A}{\sqrt{2\pi\gamma_0^2}} \exp\left[\frac{-(\omega - \Omega_0)^2}{2\gamma_0^2}\right] \quad (3)$$

where $\gamma_0 = 28.8$ meV is the laser center frequency, and $\Omega_0 = 1.57$ eV is the laser bandwidth. $K_{\text{SP}}(\omega, t < 0)$ represents the time-independent SP absorption spectrum before the pump pulse arrives. The evolution of the SP absorption spectrum after the pump pulse is injected is described by

$$K_{\text{SP}}(\omega, t \geq 0) = \frac{A}{\sqrt{2\pi\gamma^2(t)}} \exp\left[\frac{-(\omega - \Omega(t))^2}{2\gamma^2(t)}\right] \quad (4a)$$

where the time-dependent center frequency shift and bandwidth are

$$\Omega(t) = \Omega_0 + \Delta\Omega_{\text{SP}}(t) \quad (4b)$$

and

$$\gamma(t) = \gamma_0 + \Delta\gamma_{\text{SP}}(t) \quad (4c)$$

This formula ignores the effects of interband transitions, meaning that our analysis is applicable only to systems for which such transitions are negligible, such as the longitudinal SP resonances studied here.

The absorptive and dispersive parts measured in OHD-FWM experiments can be represented as

$$S_{\pi/2}(t) = -L \int d\omega P(\omega)[n_{\text{SP}}(\omega, t) - n_{\text{SP}}(\omega, t < 0)] \quad (5a)$$

and

$$S_\pi(t) = -L \int d\omega P(\omega)[K_{\text{SP}}(\omega, t) - K_{\text{SP}}(\omega, t < 0)] \quad (5b)$$

where L is the sample path length, $P(\omega)$ denotes the laser pulse spectrum, $K_{\text{SP}}(\omega, t)$ represents the absorption spectrum of the longitudinal SP, and $n_{\text{SP}}(\omega, t)$ is obtained from $K_{\text{SP}}(\omega, t)$ using

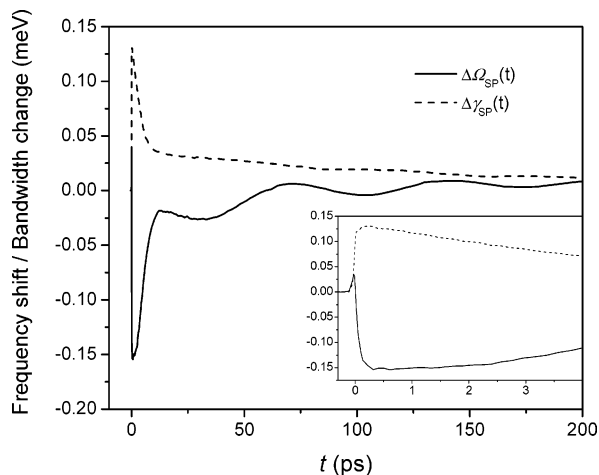


Figure 3. The calculated time-dependent frequency shift, $\Delta\Omega_{\text{SP}}(t)$, and bandwidth change, $\Delta\gamma_{\text{SP}}(t)$, of the longitudinal SP absorption of Au nanorods. The inset shows the same data at early times.

the Kramers–Kronig relation. $\Delta\Omega_{\text{SP}}(t)$ and $\Delta\gamma_{\text{SP}}(t)$ are determined such that the calculated absorptive and dispersive parts in eqs 5a and 5b reproduce the corresponding signals measured in OHD-FWM experiments.

The resulting $\Delta\Omega_{\text{SP}}(t)$ and $\Delta\gamma_{\text{SP}}(t)$ are shown in Figure 3. It should be noted that the offset at longer time results from a thermal grating, which decays on a nanosecond time scale. $\Delta\Omega_{\text{SP}}(t)$ is negative and $\Delta\gamma_{\text{SP}}(t)$ is positive; in other words, the longitudinal SP absorption at a higher electron temperature is red-shifted and is broader than the SP absorption at ambient temperature T_0 . On longer time scales, the coherent oscillation of the nanorods is observed in $\Delta\Omega_{\text{SP}}(t)$. The frequency of the SP band is modulated by changes in the aspect ratio and electron density as the nanorods contract and expand. As shown in Figures 2 and 3, the shapes of $\Delta\Omega_{\text{SP}}(t)$ and $\Delta\gamma_{\text{SP}}(t)$ are similar to those of $S_{\pi/2}(t)$ and $S_\pi(t)$, but the relative amplitudes are different. The change in probe absorption, for the laser pulses and resonance conditions used, is sensitive to broadening of the SP, while the change in refractive index is sensitive to the frequency shift of the SP.

Del Fatti et al. have previously performed femtosecond pump–probe measurements on silver nanoparticles embedded in a glass matrix.^{9,34} They measured the probe wavelength dependence of the transmission change around the SP resonance at a fixed time delay and extracted frequency shifts and broadening of the resonance by fitting the transient spectra. The values of $\Delta\Omega_{\text{SP}}(t)$ and $\Delta\gamma_{\text{SP}}(t)$ obtained in the current OHD-FWM measurements are of the same order of magnitude as their results.

3.3. Vibrational Dynamics. The coherent vibrational modes of cylindrical rods with an aspect ratio much greater than one are separated into two fundamental modes: extensional and breathing. The oscillation period, T_{ext} , and damping time constant, τ_{ext} , of the extensional mode depend on the size distribution of the rods and their elastic constants^{14,35}

$$T_{\text{ext}} = \frac{2L}{\sqrt{E/\rho}} \quad \tau_{\text{ext}} = \frac{LT_{\text{ext}}}{\sqrt{2\pi\sigma_L}} \quad (6)$$

where L and σ_L are the mean rod length and its standard deviation, E is the Young's modulus, and ρ is the material density.

Linear prediction singular-value decomposition³⁶ of the oscillatory component in the dispersive signal yields an oscil-

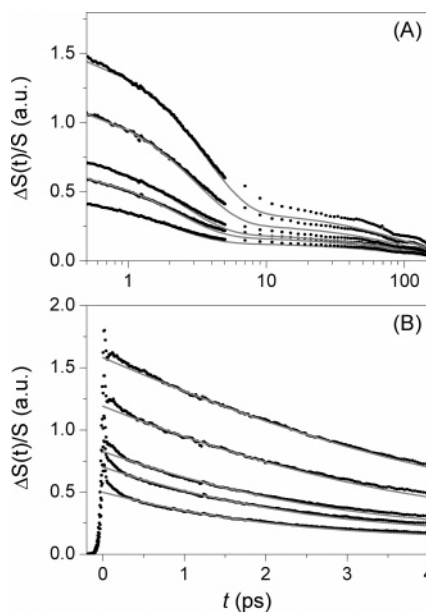


Figure 4. (A) Experimentally measured pump–probe transient-transmission data (points) and results of calculations using an explicit theory based on the effects of elevated conduction-electron and lattice temperatures (lines). The graph is plotted logarithmically in time. From top to bottom, the pump intensities are 2.1, 1.6, 1.1, 0.8, and 0.6 nJ/pulse. The probe intensity was kept fixed at 0.1 nJ/pulse. 2.1 nJ/pulse corresponds to 2.5 GW/cm². (B) The same data, plotted linearly in time, over a shorter time scale.

lation period of $T_{\text{ext}} = 71$ ps and a damping time constant of $\tau_{\text{ext}} = 98.5$ ps. For bulk Au, $E/\rho = 40.4$ kbar·cm³/g, giving an oscillation period of $T_{\text{ext}} = 52$ ps for the nanorods used in the current experiment ($L = 52.6 \pm 7.3$ nm). The experimentally measured T_{ext} is longer than the value predicted from the model calculation, most likely due to differences between the real nanorod shapes and the perfect cylinders assumed in the model.

The damping of the oscillation is mainly determined by the inhomogeneous size distribution of the nanorods in the sample. Since the oscillation period of the coherent extensional mode depends linearly on the length of the nanorods, as shown in eq 6, the nanorods with different sizes oscillate with different periods, resulting in dephasing of the signal. Using the measured length distribution of the nanorods in the sample results in an expected damping time constant of $\tau_{\text{ext}} = 84$ ps, compared to a measured damping time of $\tau_{\text{ext}} = 98.5$ ps. The pump laser excites only a subset of nanorods within the laser spectrum, since the homogeneous linewidth is narrow.² Therefore, the dispersion of sizes within this subset is less than that of the sample as a whole, accounting for the longer measured dephasing time.

4. Pump–Probe Transient-Transmission Measurements

Femtosecond pump–probe transient-transmission measurements were performed for pump pulse energies from 0.4 to 2.1 nJ, as shown in Figure 4. The center frequency of the laser pulse was 790 nm, resonant with the longitudinal SP absorption. The probe intensity was fixed at 0.1 nJ/pulse.

4.1. Effects of Changes in Electron and Phonon Temperatures. Our first analysis of the pump–probe data involves an explicit calculation of thermally induced changes in the optical properties of the nanorods. First, part of the energy of the incident pump laser pulse is absorbed by the plasmons, which are assumed to instantaneously decay, resulting in heating of the conduction electrons in the rod. The conduction electrons

exchange heat with the Au lattice through electron–phonon scattering, and the lattice exchanges heat with its surroundings through phonon–phonon scattering. The heat capacity of the surroundings is taken to be effectively infinite, so that the final state is a return of the electrons and the phonons to room temperature, T_0 .

The processes described above can be modeled by treating the electrons, the lattice, and the surroundings as three coupled thermal reservoirs. We assume that the three heat baths are in thermal equilibrium at all times. The temperatures of the electrons, T_e , and of the lattice, T_l , can then be described with the following pair of differential equations:¹¹

$$C_e(T_e) \frac{\partial T_e}{\partial t} = -G_{e-\text{ph}}(T_e - T_l) \quad (7)$$

$$C_l \frac{\partial T_l}{\partial t} \approx G_{e-\text{ph}}(T_e - T_l) - G_{\text{ph-ph}}(T_l - T_o) \quad (8)$$

Here, $C_e(T_e)$ and C_l are the heat capacities of the electrons and the lattice (i.e., phonons), respectively, and $G_{e-\text{ph}}$ and $G_{\text{ph-ph}}$ are the coupling coefficients between the electrons and the lattice and between the lattice and surroundings, respectively. The electron heat capacity is proportional to temperature: $C_e(T_e) = \gamma_e T_e$, with $\gamma_e = 71.5$ J m⁻³ K⁻².^{37,38} The lattice heat capacity, on the other hand, is taken to be $C_l \approx 3k_B n$, where k_B is Boltzmann's constant and $n = 5.9 \times 10^{28}$ m⁻³ is the atomic density of Au.³⁸ We take $G_{e-\text{ph}} = 1.9 \times 10^{17}$ W/m³ K, to agree with previous measurements on Au nanoparticles.¹⁶ On the other hand, $G_{\text{ph-ph}}$ depends on the details of the thermal coupling between the rods and their surroundings, including the thermal conductivity of the solvent and the effects of the layer of surfactant that covers the rods. This parameter is thus left adjustable, to match the experimental data.

With these parameters, eqs 7 and 8 can readily be solved numerically. The initial conditions are that $T_l = T_o$, while T_e is given by the energy absorbed from the pump laser pulse by the nanorod. This absorbed energy is determined by the incident pulse energy, the laser spot size, and the calculated optical absorption cross section of the nanorod. The measured pulse energy is scaled by a constant factor in order to take into account systematic uncertainties in the laser spot size and optical attenuation between the point where the energy is measured and the area where the pump and probe interact.

The effect of the changing T_e and T_l is to change the dielectric function $\epsilon(\omega)$ of the Au that makes up the nanorods. The dielectric function is taken to be^{39–41}

$$\epsilon(\omega, T_e, T_l) = \left[1 - \frac{\omega_p(T_l)^2}{\omega^2 - i\gamma(T_e, T_l)\omega} \right] + \epsilon^{d-c}(\omega, T_e) \quad (9)$$

The first term is the Drude response due to free conduction electrons, and the second term is due to electronic transitions between lower-lying d-band states and available conduction-band states above the Fermi level. In the Drude term, ω_p is the bulk plasma frequency, given by $\omega_p = \sqrt{4\pi n q^2/m_{\text{eff}}}$, where n is the electron density, taken to be equal to the atomic density; q is the electronic charge; and m_{eff} is the effective mass of the conduction electrons.⁴⁰ The bulk plasmon damping term, $\gamma(T_e, T_l)$, is adjusted to fit the room-temperature dielectric constants of ref 42. The dependence of the damping on the lattice temperature is assumed to be linear, while the dependence of the damping on electron temperature is calculated according to the phenomenological formula given in ref 12.

The term in the dielectric function due to interband transitions is calculated according to the theory described in ref 39, using parameters from refs 39–41. When considering wavelengths near 800 nm, it is necessary to consider transitions both at the *L* point and the *X* point in the Brillouin zone.⁴⁰ The calculations give the interband contribution to the dielectric function within a constant proportional to the interband matrix element, which is adjusted to give room-temperature dielectric constants that match the data in ref 42. The effect of increasing electron temperature, T_e , is to spread out the distribution of electrons about the Fermi energy, E_F , increasing the number of available states for interband transitions to states below E_F , and to broaden the Drude response due to increased electron scattering.

Once the time-dependent electron and lattice temperatures and the temperature-dependent dielectric functions have been calculated, all that is left to determine is the optical response of the nanorods for a particular dielectric function. The optical response is calculated in the quasi-static limit, assuming that the dimensions of the nanorods are small compared to the optical wavelength.³ The rods are approximated as prolate ellipsoids. The optical extinction of the solution of nanorods (i.e., the attenuation that the probe pulse experiences) is the sum of the absorption and scattering from all of the nanorods in solution, and is integrated over the random orientation of the rods as well as their inhomogeneous distribution in shape. For each delay time after excitation by the pump laser pulse, the electron and lattice temperatures are calculated, the resulting dielectric functions are determined, and the resulting extinction spectrum is calculated. This spectrum is then integrated over the measured laser spectrum to give the total attenuation of the probe pulse. This attenuation is compared to the attenuation at room temperature to finally give the pump–probe signal as a function of time delay.

Figure 4 shows the calculated results for a number of pulse energies. All the data are fitted with only three free parameters: (1) the scaling factor between the measured pulse energy and the energy at the interaction volume; (2) the thermal coupling coefficient between the Au lattice and its surroundings; and (3) an overall scaling factor for the response. Agreement is good over the range of pulse energies considered, although some deviation is seen at longer delays, particularly for the highest pump powers. The degradation of the agreement may be due to local heating of the solution surrounding the nanorods. We note that we have also neglected the effects of lattice dilation on interband transition energies and on electron density.

Despite the good general agreement, there are three clear features in the experimental data that are not reproduced in the calculation: (1) a time-resolution-limited spike at zero time delay; (2) a decaying component at short delays, with a time constant of approximately 170 fs; and (3) coherent oscillations at longer delays, with a period of 71 ps, as described above.

4.2. Phenomenological Response Function. To take into account all of the dynamics observed experimentally, we introduce a phenomenological response function, $R(t)$, to describe the change in the transmission of the sample in response to the incident pump pulse. The measured transient change in transmission, $\Delta S(t)/S$, is a convolution of the material response function with the instrumental response function, $G_0^{(2)}(t)$

$$\frac{\Delta S(t)}{S} = \int dt [\delta G_0^{(2)}(t) + G_0^{(2)}(t)R(t-t)] \quad (10)$$

where δ represents a zero-delay component due to the coherent nonlinear response of the nanorods.

The response function, $R(t)$, is constructed using the model in the previous section as a starting point. Equations 7 and 8, describing the coupled electron, phonon, and surrounding heat baths, are approximated by assuming that the excitation of the rods is relatively weak, so that the initial rise in the electron temperature is relatively small. It is further assumed that the time scales over which the electrons reach equilibrium with the lattice and over which the lattice reaches equilibrium with the surroundings are sufficiently different, so that the two processes can be considered to be sequential. (This separation of time scales is justified by the detailed modeling results described above.) The initial decay in the electron temperature due to electron–phonon coupling can then be approximated as a single exponential, with a decay time τ_{e-ph} . The lattice temperature will initially rise with the same time constant, due to heat transfer from the electrons, and then decay with the time constant τ_{ph-ph} , due to heat transfer to the surroundings.

We add an initial, quickly decaying component to this thermal response function, to match the observed dynamics. We tentatively ascribe this component to the effects of nonthermal electrons. That is, the plasmons that are excited by the pump pulse decay into an electron distribution which differs from a thermal distribution and which takes some time to reach internal thermal equilibrium. The validity of this assignment is discussed further below. In this model, the electron distribution function is written as a sum of nonthermal and thermal parts^{4,37}

$$f = f_{\text{nonthermal}}(E, t) + f_{\text{thermal}}[E, T_e(t)] \quad (11)$$

where $T_e(t)$ is the electron temperature. We assume that the relaxation of the nonthermal distribution into a thermal distribution is fast compared to the electron–phonon coupling. In this case, the decay of the nonthermal electron population into a thermal population is accounted for by a decaying exponential with a time constant τ_{th} . However, it is also necessary to take into account direct energy transfer from the nonthermal electron population to the lattice, with a time constant given by $1/\tau_{NT} = 1/\tau_{th} + 1/\tau_{e-ph}$.⁴

The last component that needs to be included in the response function is the oscillation due to the coherent vibration of the lattice, as described above. This is simply done by adding an oscillatory component with a frequency ω and a phase ϕ .

Including all of the above components, the final response function is written as

$$R(t) = H(t)[A_{NT} e^{-t/\tau_{NT}} + A_{Th} e^{-t/\tau_{e-ph}}(1 - e^{-t/\tau_{th}}) + A_{ph-ph}(1 - e^{-t/\tau_{e-ph}}) e^{-t/\tau_{ph-ph}} + A_{osc} e^{-t/\tau_{osc}} \cos(\omega t + \phi)] \quad (12)$$

where $H(t)$ is the Heaviside step function.

All of the parameters in eqs 10 and 12 were determined by nonlinear least-squares (NLLS) fitting. Figure 5 shows an example of the NLLS fitting results, and the fitting parameters are listed in Table 1. The time constants are plotted against the intensity of the pump pulse in Figure 6.

A. Coherent Response. We attribute the zero-delay spike to coherent nonlinearities associated with the SP oscillation. On the basis of the homogeneous line width,² the dephasing time of the SP is shorter than the duration of the laser pulses. Any nonlinearity in the plasmon oscillation will thus show up as a spike with the duration of the laser pulse, due to induced changes in the resonance as well as coupling of the wavelength-degenerate pump pulse into the probe direction.⁴³ We note that the solvent nonresonant nonlinear response is negligible for the laser energies used.

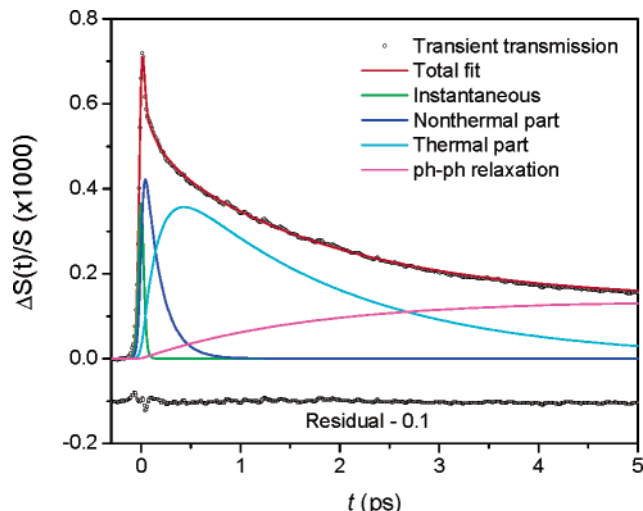


Figure 5. Nonlinear least-squares (NLLS) fit to the transient transmission signal for 0.63 nJ excitation pulses. The dynamics due to electron thermalization, electron–phonon relaxation, and phonon–phonon relaxation are well-separated in time. An instantaneous response is also present at zero delay. The residual to the fit is shown offset from zero, for clarity.

TABLE 1: Results of Nonlinear Least Square (NLLS) Fit to the Transient-Transmission Data Shown in Figure 5

pulse energy	δ	A_{NT}	τ_{th} (ps)	A_{Th}	τ_{e-ph} (ps)	A_{ph-ph}	τ_{ph-ph} (ps)
0.42 nJ	0.26	6.2	0.20	4.7	1.6	1.5	120
0.63 nJ	0.37	8.8	0.18	7.3	1.8	2.1	120
0.84 nJ	0.45	11	0.16	10	2.0	2.8	120
1.05 nJ	0.54	13	0.17	12	2.1	3.3	120
1.6 nJ	0.66	18	0.16	18	2.6	4.7	120
2.1 nJ	0.80	24	0.75	25	2.9	6.2	120

Coherent nonlinearities in the SP response presumably reflect anharmonic components in the SP oscillation. Deviations from simple harmonic oscillation are likely due to confinement of electrons by the boundaries of the rod; such confinement-induced effects have also been invoked to explain the generation of third-harmonic radiation by resonantly driven plasmons.^{44,45} This coherent response could not be observed in previous experiments, in which the nanoparticles were excited at wavelengths away from the SP resonances.

B. Electron Thermalization. As shown in Figure 6A, the time constant, τ_{th} , for electron thermalization (i.e., energy exchange among electrons) is independent of the energy of the pump pulse and equal to 170 fs, up to pump pulse energies of about 1.6 nJ. At pump energies of 2.1 nJ and above, τ_{th} increases dramatically. The unusual behavior for higher pump powers will be discussed further below.

Electron thermalization has been studied in several experiments involving excitation at energies away from the plasmon resonance. Various thermalization times have been reported: 700 fs for 30-nm Au films, using time-resolved photoemission spectroscopy;³⁷ and 500 fs for 20-nm films, using transient transmission and reflectivity measurements.⁴ More closely related are femtosecond transient absorption spectroscopy measurements performed by Link et al. on Au nanoparticles with an average diameter between 9 and 48 nm.⁷ They reported that the electron thermalization occurred on a 500 fs time scale with low power excitation, and was independent of nanoparticle size. Voisin et al. have performed probe-wavelength-dependent measurements for gold and silver nanoparticles with average sizes ranging from 2 to 26 nm.⁴⁶ Electron thermalization times were measured to be 250 and 450 fs in silver and gold nanoparticles, respectively.

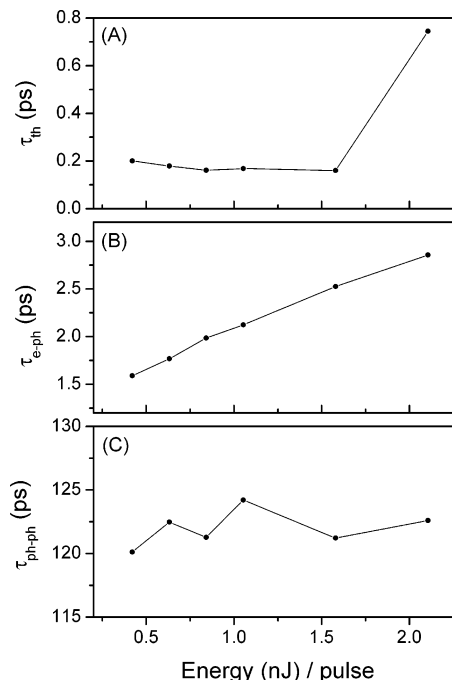


Figure 6. Pulse intensity dependence of time constants for (A) electron thermalization, (B) electron–phonon relaxation, and (C) phonon–phonon relaxation.

These previous studies, however, involved excitation with laser pulses whose wavelengths were far from surface plasmon resonances. Absorption of these pulses involve promotion of conduction electrons from below the Fermi surface to above, resulting in a highly nonthermal nascent distribution of electron energies.^{12,47} In the present study, by contrast, the incident laser pulses resonantly excite surface plasmons, which lose their energy to conduction electrons through Landau damping,⁴⁸ resulting in a different distribution of electron energies. Photoemission spectroscopy experiments on Ag nanoparticles and rough films, for example, have shown very different electron distributions for excitation on-resonance and off-resonance with surface plasmons:^{49,50} off-resonant excitation results in the uniform promotion of a block of electrons by the photon energy, while resonant excitation results in an approximately exponential distribution of electron energies. This may account for the shorter thermalization time that we measure compared to earlier experiments.

On the other hand, the initial electron energies produced by resonant excitation of plasmons have been measured by photoemission to be close to a Fermi distribution. It is perhaps surprising, then, to see any signal due to a nonthermal electron population, meaning that the transient signal we observe may have another origin. One possibility is that the incident laser pulses excite two-photon transitions between d bands and the conduction band. This would imply, though, a 170-fs recombination time for the excited electron–hole pairs, which is significantly longer than expected.^{51,52} We thus tentatively assign the signal to electron thermalization; additional experiments will be necessary to confirm this assignment.

C. Electron–Phonon Relaxation. Following electron thermalization, the electrons cool by exchanging heat with the lattice. The electron heat capacity is temperature-dependent: $C_e(T_e) = \gamma_e T_e$, with $\gamma_e = 71.5 \text{ J m}^{-3} \text{ K}^{-2}$. By contrast, the lattice heat capacity, C_l , is nearly independent of temperature under our experimental conditions. For short delays, the thermal coupling between the rod and the surroundings can be neglected. Equations 7 and 8, describing the evolution of the electron and

lattice temperatures occurring on picosecond time scales, then simplify to

$$\frac{\partial(T_e - T_l)}{\partial t} \approx -\beta(T_e - T_l) \quad (13)$$

where $\beta = G[1/C_e(T_e) + 1/C_l(T_l)]$. For a weak perturbation, $C_e(T_e)$ can be approximated by $C_e(T_0)$, leading to an exponential decay of the electron temperature, with a time constant $\tau_{e-ph}^0 \equiv 1/\beta = \gamma_e T_0/G_{e-ph}$. For larger perturbations, the electron–phonon relaxation is nonexponential: it is initially slow, gets faster, and finally becomes exponential, with a final time constant of τ_{e-ph}^0 .¹¹

As shown in Figure 6B, the fitted value of τ_{e-ph} increases linearly with increasing pump pulse intensity. The intensity-dependent decay time reflects small deviations from the assumption of a temperature-independent electron heat capacity. A reasonably accurate value of τ_{e-ph} can be determined by extrapolating τ_{e-ph} to zero pump intensity, giving an intrinsic electron–phonon relaxation time $\tau_{e-ph}^0 = 0.79 \pm 0.03$ ps. This implies an electron–phonon coupling constant $G_{e-ph} = \gamma_e T_0/\tau_{e-ph}^0 = (2.5 \pm 0.1) \cdot 10^{16}$ W/m³–K, in good agreement with the results reported for Au nanoparticles^{6,7,16,17} and bulk Au.⁴

D. Phonon–Phonon Relaxation. The energy exchange between the particle and the surroundings occurs by phonon–phonon coupling. Since the lattice heat capacity, C_l , and the heat capacity of the surroundings, C_s , are not strongly temperature-dependent, the time constant for the phonon–phonon relaxation is approximately equal to a constant value of $1/\tau_{ph-ph}$, assuming that the temperature changes of the solvent can be neglected. This prediction is in excellent agreement with our results, as shown in Figure 6C. The average time constant for the phonon–phonon relaxation is 122 ± 2 ps.

4.3. Electron Dynamics at Higher Pump Intensities. Figure 7A shows the result of pump–probe transient transmission measurements at higher pump intensities, using a similar Au nanorod sample. The best fitted values of τ_{th} and τ_{e-ph} for these data are shown in Figures 7B and 7C; a marked change in behavior is seen when the pump-pulse energy exceeds 2.0 nJ.

For high pulse energies, the SP oscillation is strongly excited, implying a large amplitude of coherent collective electron oscillation. It is reasonable to suppose that there will be a corresponding increase in mechanisms that lead to damping of the SP. At the same time, additional nonlinear mechanisms are likely to become active. For example, photoemission experiments have shown that plasmon excitation in rough Ag films can lead to the production of highly energetic electrons.⁵³ The overall effect is to reduce the magnitude of the coherent nonlinear response and to alter the short-time dynamics of the conduction–electron distribution.

Recently, optical nonlinearities of single Au nanorods were investigated by measuring scattering from the nanorods in the strong perturbation regime.² A very large, ultrafast nonlinearity was observed, and the mechanism for the early-time dynamics was indistinguishable from that for the longer time dynamics. This is consistent with the supposition that, under strong excitation, the SP dephasing and internal electron thermalization occur very rapidly, well within the 40-fs excitation-pulse duration employed here.

The phenomenological response function of eq 12, in which the relaxation dynamics are described as a sum of sequential, exponential processes, is thus valid only in the weak perturbation regime and cannot be directly applied to the strong perturbation regime. Under the present experimental conditions, the phe-

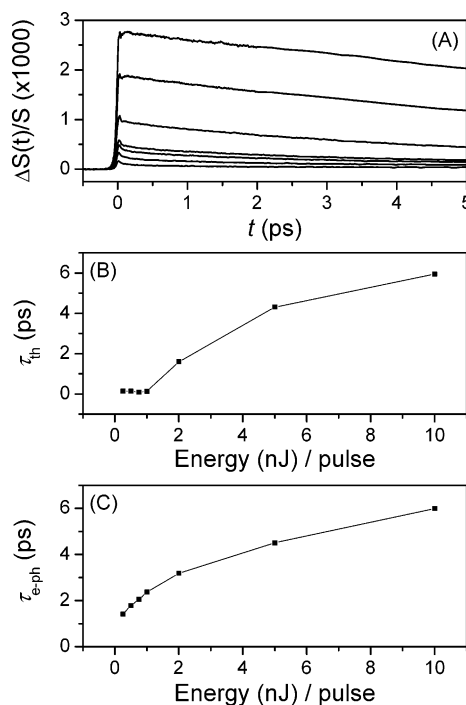


Figure 7. (A) Pump–probe transient transmission measurements for higher pump-pulse energies. From top to bottom, the pump intensities are 10.0, 5.0, 2.0, 1.0, 0.75, 0.50, and 0.25 nJ/pulse. The probe energy was kept at 0.1 nJ/pulse. (B) Pulse intensity dependence of time constants for electron thermalization. (C) Time constants for electron–phonon relaxation.

nomenological model is applicable for pump intensities below 2.0 nJ (2.5 GW/cm²).

5. Conclusions

Au nanorods are synthesized via a seed-mediated growth process, and their longitudinal surface-plasmon absorption is tuned away from the interband transition. It is therefore possible to selectively excite and probe the longitudinal SP mode in the Au nanorods, with negligible excitation of d-band electrons. Changes in the response of the SP resonance thus serve as a direct probe of the distribution of conduction electrons in the nanorods and the dynamics of this distribution.

OHD-FWM spectroscopy provides selective measurements of the dispersive and absorptive parts of the signal, which allows the dynamics to be described in terms of the frequency shift and broadening of the SP absorption upon excitation of the longitudinal SP mode. In addition, a coherent vibrational oscillation is observed, primarily in the dispersive part of the signal.

Electron dynamics are systematically investigated by pump–probe transient-transmission measurements. An explicit calculation is able to reproduce the observed signal due to heating of conduction electrons and lattice phonons, for relatively low pump powers. Phenomenological fitting is necessary to take into account an instantaneous coherent signal and a decaying signal with a time constant of 170 fs. The instantaneous signal is attributable to anharmonic components in the SP oscillation. The decaying signal is ascribed to electron thermalization; however, additional studies are required to exclude two-photon-excited interband transitions or other mechanisms.

At high pump intensities, the dynamics of electron thermalization and electron–phonon coupling show significant deviations from their behavior at lower pump intensities, and the

simple phenomenological fitting model is no longer able to accurately describe the data.

Acknowledgment. This work is supported by the National Science Foundation (CHE0317009 and CHE0616663). We also acknowledge partial support from the University of Chicago MRSEC (DMR0213745). M.P. was supported by the Grainger Postdoctoral Fellowship in Experimental Physics from the University of Chicago. We thank M. Hershberger for assistance with the measurements and Prof. H. Petek for helpful discussions.

References and Notes

- (1) Michaels, A. M.; Nirmal, M.; Brus, L. E. *J. Am. Chem. Soc.* **1999**, *121*, 9932.
- (2) Pelton, M.; Liu, M.; Park, S.; Scherer, N. F.; Guyot-Sionnest, P. *Phys. Rev. B* **2006**, *73*, 155419.
- (3) Bohren, C. F.; Huffman, D. R. *Absorption and Scattering of Light by Small Particles*; John Wiley & Sons: New York, 1983.
- (4) Sun, C.-K.; Vallée, F.; Acioli, L. H.; Ippen, E. P.; Fujimoto, J. G. *Phys. Rev. B* **1994**, *50*, 15337.
- (5) Ahmadi, T. S.; Logunov, S. L.; El-Sayed, M. A. *J. Phys. Chem.* **1996**, *100*, 8053.
- (6) Hodak, J. H.; Martini, I.; Hartland, G. V. *J. Phys. Chem. B* **1998**, *102*, 6958.
- (7) Link, S.; Burda, C.; Wang, Z. L.; El-Sayed, M. A. *J. Chem. Phys.* **1999**, *111*, 1255.
- (8) Link, S.; El-Sayed, M. A. *J. Phys. Chem. B* **1999**, *103*, 8410.
- (9) Del Fatti, N.; Vallée, F.; Flytzanis, C.; Hamanaka, Y.; Nakamura, A. *Chem. Phys.* **2000**, *251*, 215.
- (10) Voisin, C.; Christofilos, D.; Del Fatti, N.; Vallée, F.; Prevel, B.; Cottancin, E.; Lerme, J.; Pellarin, M.; Broyer, M. *Phys. Rev. Lett.* **2000**, *85*, 2200.
- (11) Fatti, N. D.; Voisin, C.; Achermann, M.; Tzortzakis, S.; Christofilos, D.; Vallée, F. *Phys. Rev. B* **2000**, *61*, 16956.
- (12) Voisin, C.; Fatti, N. D.; Christofilos, D.; Vallée, F. *J. Phys. Chem. B* **2001**, *105*, 2264.
- (13) Link, S.; El-Sayed, M. A. *Annu. Rev. Phys. Chem.* **2003**, *54*, 331.
- (14) Hartland, G. V. *Phys. Chem. Chem. Phys.* **2004**, *6*, 5263.
- (15) Del Fatti, N.; Vallée, F. *Appl. Phys. B: Laser Opt.* **2001**, *73*, 383.
- (16) Arbouet, A.; Voisin, C.; Christofilos, D.; Langot, P.; Del Fatti, N.; Vallée, F. *Phys. Rev. Lett.* **2003**, *90*, 177401.
- (17) Link, S.; Burda, C.; Mohamed, M. B.; Nikoobakht, B.; El-Sayed, M. A. *Phys. Rev. B* **2000**, *61*, 6086.
- (18) Bigot, J.-Y.; Halte, V.; Merle, J.-C.; Daunois, A. *Chem. Phys.* **2000**, *251*, 181.
- (19) Hodak, J. H.; Henglein, A.; Hartland, G. V. *J. Phys. Chem. B* **2000**, *104*, 9954.
- (20) Nikoobakht, B.; El-Sayed, M. A. *Chem. Mater.* **2003**, *15*, 1957.
- (21) Liu, M.; Guyot-Sionnest, P. *J. Phys. Chem. B* **2004**, *108*, 5882.
- (22) Liau, Y.-H.; Unterreiner, A. N.; Arnett, D. C.; Scherer, N. F. *Appl. Opt.* **1999**, *38*, 7386.
- (23) Ruggiero, A. J.; Scherer, N. F.; Mitchell, G. M.; Fleming, G. R.; Hogan, J. N. *J. Opt. Soc. Am. B* **1991**, *8*, 2061.
- (24) Norris, T. B. *Opt. Lett.* **1992**, *17*, 1009.
- (25) Maznev, A. A.; Nelson, K. A. *Opt. Lett.* **1998**, *23*, 1319.
- (26) Goodno, G. D.; Dadusc, G.; Miller, R. J. D. *J. Opt. Soc. Am. B* **1998**, *15*, 1791.
- (27) Khalil, M.; Demirdoven, N.; Golonzka, O.; Fecko, C. J.; Tokmakoff, A. *J. Phys. Chem. A* **2000**, *104*, 5711.
- (28) Xu, Q.-H.; Ma, Y.-Z.; Fleming, G. R. *Chem. Phys. Lett.* **2001**, *338*, 254.
- (29) Xu, Q.-H.; Ma, Y.-Z.; Fleming, G. R. *J. Phys. Chem. A* **2002**, *106*, 10755.
- (30) Park, S.; Kim, J.; Scherer, N. F. Manuscript in preparation, 2006.
- (31) Heilweil, E. J.; Hochstrasser, R. M. *J. Chem. Phys.* **1985**, *82*, 4762.
- (32) Bloemer, M. J.; Haus, J. W.; Ashley, P. R. *J. Opt. Soc. Am. B* **1990**, *7*, 790.
- (33) Xu, Q.-H.; Ma, Y.-Z.; Stiopkin, I. V.; Fleming, G. R. *J. Chem. Phys.* **2002**, *116*, 9333.
- (34) Del Fatti, N.; Flytzanis, C.; Vallée, F. *Appl. Phys. B: Laser Opt.* **1999**, *68*, 433.
- (35) Hu, M.; Wang, X.; Hartland, G. V.; Mulvaney, P.; Juste, J. P.; Sader, J. E. *J. Am. Chem. Soc.* **2003**, *125*, 14925.
- (36) Vohringer, P.; Scherer, N. F. *J. Phys. Chem.* **1995**, *99*, 2684.
- (37) Fann, W. S.; Storz, R.; Tom, H. W. K.; Bokor, J. *Phys. Rev. Lett.* **1992**, *68*, 2834.
- (38) Ashcroft, N. W.; Mermin, N. D. *Solid State Physics*; Brooks/Cole: New York, 1976.
- (39) Rosei, R. *Phys. Rev. B* **1974**, *10*, 474.
- (40) Guerrisi, M.; Rosei, R.; Winsemius, P. *Phys. Rev. B* **1975**, *12*, 557.
- (41) Rosei, R.; Antonangeli, F.; Grassano, U. M. *Surf. Sci.* **1973**, *37*, 689.
- (42) Johnson, P. B.; Christy, R. W. *Phys. Rev. B* **1972**, *6*, 4370.
- (43) Gumy, J.-C.; Nicolet, O.; Vauthey, E. *J. Phys. Chem. A* **1999**, *103*, 10737.
- (44) Fomichev, S. V.; Popruzhenko, S. V.; Zaretsky, D. F.; Becker, W. *Opt. Express* **2003**, *11*, 2433.
- (45) Lippitz, M.; van Dijk, M. A.; Orrit, M. *Nano Lett.* **2005**, *5*, 799.
- (46) Voisin, C.; Christofilos, D.; Loukakos, P. A.; Fatti, N. D.; Vallée, F.; Lerme, J.; Gaudry, M.; Cottancin, E.; Pellarin, M.; Broyer, M. *Phys. Rev. B* **2004**, *69*, 195416.
- (47) Fann, W. S.; Storz, R.; Tom, H. W. K. *Phys. Rev. B* **1992**, *46*, 13592.
- (48) Lifschitz, E. M.; Pitaevskii, L. P. *Physical Kinetics*; Permagon Press: New York, 1981.
- (49) Merschdorf, M.; Pfeiffer, W.; Thon, A.; Voll, S.; Gerber, G. *Appl. Phys. A: Mater. Sci. Process.* **2000**, *71*, 547.
- (50) Kubo, A.; Onda, K.; Petek, H.; Sun, Z.; Jung, Y. S.; Kim, H. K. *Nano Lett.* **2005**, *5*, 1123.
- (51) Varnavski, O. P.; Mohamed, M. B.; El-Sayed, M. A.; Goodson, T., III. *J. Phys. Chem. B* **2003**, *107*, 3101.
- (52) Varnavski, O. P.; Goodson, T., III.; Mohamed, M. B.; El-Sayed, M. A. *Phys. Rev. B* **2005**, *72*, 235405.
- (53) Banfi, G.; Ferrini, G.; Peloi, M.; Parmigiani, F. *Phys. Rev. B* **2003**, *67*, 035428.